Lawrence Berkeley National Laboratory

Title

Black carbon enriches short-range-order ferrihydrite in Amazonian Dark Earth: Interplay mechanism and environmental implications

Permalink

Authors

Weng, Yi-Tse
Rathod, Jagat
Liang, Biqing
et al.

Publication Date

2020-07-01

Peer reviewed

1 **Black Carbon enriches Short-Range-Order Ferrihydrite in Amazonian Dark Earth: Interplay**

2 **Mechanism and Environmental Implications**

3 Yi-tse Weng[1], Chun-Chieh Wang[2], Jagat Rathod[1], Biqing Liang[1, *], Yoshiyuki Iizuka[3], Nobumichi
4 Tamura[4], Chi-Liang Chen[5], Yao-Chang Lee[6], Ting-Shan Chan[5]

5

6 [1] Department of Earth Sciences, National Cheng Kung University, Tainan, Taiwan

7 [2] Biomedical & Molecular Imaging Group, National Synchrotron Radiation Center, Hsinchu,

8 Taiwan

9 [3] Institute of Earth Sciences, Academia Sinica, Taipei, Taiwan

10 [4] Advance Light Source, Lawrence Berkeley National Lab, Berkeley, CA, USA

11 [5] X-ray Absorption Group, National Synchrotron Radiation Center, Hsinchu, Taiwan

12 [6] X-ray and IR Imaging Group, National Synchrotron Radiation Center, Hsinchu, Taiwan

13 *Correspondence: Biqing Liang

14 Email:liangbq@gs.ncku.edu.tw, Tel: 886-6-2757575 ext 65433

15

16 **ABSTRACT**

17 Black carbon (BC, biochar) has received appreciable research attention due to its potential in

18 sequestrating C and improving soil fertility. Organo-mineral interaction plays a key role in BC long-

19 term stabilization and resistance to degradation in natural environments. To investigate the

20 mechanism of organo-mineral interaction, we studied the physicochemical features of BC and

21 associated minerals in historical BC-rich Amazonian Dark Earth (ADE) using synchrotron-based

22 microscopic (TXM) and spectroscopic (FTIR, XAS and XRD) approaches. More than 100% higher

23 content of poorly crystalline minerals was found in BC-rich ADE, compared to the adjacent tropical

24 soils. Reactive short-range-order (SRO) ferrihydrite, in nano-clusters and layers, were observed as

25 the key minerals interplaying with BC surface. Linear combination fitting (LCF) of k-spacing in X-

26 ray Absorption Spectra (XAS) revealed that ferrihydrite contributed up to 81.1% of Fe-minerals in

BC, whereas the rest 18.9% was hematite. The adjacent soil had higher goethite content (41.7%) than ADE (19.9%). A small but distinct peak was observed at 5.7 Å^{-1} in the EXAFS k oscillation of BC, which was characteristic of Fe-O-C bonds. No Fe-C path (or Fe-O-C bond) was successfully fitted by XAS analyses for Fe coordination when obvious peak downshift of the first (Fe-Fe^1) shell was observed, suggesting the availability of inner-sphere Fe-C complexation was limited to BC surface and interphase region. The main minerals on BC via organo-mineral complexation was SRO ferrihydrite instead of corner-sharing FeO_6 octahedra or Fe oligomers. The coordination number (CN) of the first (Fe-Fe^1) and second (Fe-Fe^2) shell was higher in BC (2.36±0.51; 1.30±0.65), compared to ADE (1.68±0.56; 0.47±0.40). A higher CN in BC denoted a higher degree of order in coordination between neighboring Fe mineral crystals. Black C limited the progressive aging of poorly crystalline Fe phases and enriched SRO ferrihydrite to a great extent in a redox fluctuating and high-leaching environment. Our research supported that the transformation of SRO ferrihydrite to more crystalline Fe oxides were controlled by the local pH environment in ADE and adjacent soil. Broad and pronounced FTIR bands were observed within 1200-1400 cm^{-1} and 1650-1730 cm^{-1} in BC, pointing to a significant level of organo-mineral complexation. Strong signal of complexed phenolic functional groups (aryl-OH, 1241 cm^{-1}) and distinct band of inner sphere Fe-aromatic C complexation was identified at 1380-1384 cm^{-1}. The negatively charged reactive functional groups on BC surface interacted with positively charged SRO ferrihydrite through covalent bond, ligand exchange and cation bridging. The enrichment of poorly crystalline minerals could have a positive feedback on the long-term stabilization of BC and warrants further research. The scale up application of biochar into agri- and ecological system may have a long lasting impact on the transformation of associated minerals.

Keywords

Black carbon, Biochar, Organo-mineral interaction mechanism, Short-range-order (SRO) mineral,

52   Ferrihydrite, XAS, EXAFS

53

1. INTRODUCTION

Black carbon (BC, biochar) has received appreciable study attention worldwide due to its potential in sequestrating carbon, improving soil fertility improvement and remediating environmental pollutant (Kuhlbusch, 1998; Liang et al., 2006; Ramanathan and Carmichael, 2008; Schmidt, 2004). Generally considered highly stable due to their inherent aromaticity, both chemical recalcitrance and physical protection via interactions with mineral are suggested indispensable for their longevity (Cusack et al., 2012; Jones and Edwards, 1998; Liang et al., 2008; Torn et al., 1997; Vogel et al., 2014). It remained contentious about the real residence time of BC in natural environments, especially for buried BC from a wide variety of sources and pyrolysis conditions (Wang et al., 2016). The reactive functional groups (especially phenolic-C and carboxyl-C) on BC surface make them susceptible to biotic and abiotic degradation, and this may explain why the content of BC in soil hasn't increased dramatically over time (Brodowski et al., 2005; Hockaday et al., 2006; Liang et al., 2006). Whereas, the reactive surfaces of BC provide a platform for interaction with reactive minerals, either by strong chemical association, physical protection, or both (Chen et al., 2014a; Chen et al., 2016; Mikutta et al., 2006; Mikutta et al., 2007; Torn et al., 1997; Vogel et al., 2014; Weng et al., 2018). The chemical nature of BC and affinity with associated minerals will determine the extent of organo-mineral association, which largely dependent on whether the minerals are poorly crystalline and bearing proper charges or not (Mikutta et al., 2005; Mikutta et al., 2007). Stabilization of organic C by interaction with poorly crystalline minerals and polymeric metal species was recognized as the most important mechanism for C preservation (Mikutta et al., 2006; Torn et al., 1997). With a high specific surface area (~800 m^2 g^{-1}) and reactivity, short-range-order (SRO) ferrihydrite has been considered one of the most competent Fe (hydr)oxides for forming organo-mineral associations (Eusterhues et al., 2005). However, due to their submicron size and poor crystallinity, the confirmation of some SRO and nano-crystalline minerals in natural context has challenged traditional X-ray diffraction (XRD) and spectroscopic techniques. For example, the crystalline domain of ferrihydrite was normally less than 10 nm (Cornell and Schwertmann, 1996),

and it is extremely difficult to obtain a well resolved scattering/diffraction pattern directly, especially when the concentration is at low concentrations. And this may explain why SRO minerals have been overlooked in natural environment, whereas mainly post-transformed products such as goethite and hematite were detected.

Preferential interactions between reactive Fe oxides and aromatic organic C were reported (Kaiser, 2003; Riedel et al., 2013), though the phases of natural precipitated Fe (hydr)oxides were not characterized or confirmed. Plant-derived aromatic and pyrogenic compounds were preferentially retained by Fe (hydr)oxides (Riedel et al., 2013; Eusterhues et al., 2011). Iron oxides precipitated from redox cycle specifically protected aromatic lignin constituent but not the bulk soil organic C, and Fe oxide-lignin interactions were proposed a specific yet to be resolved mechanism for recalcitrant C stabilization (Hall et al., 2016).

Among the major mechanisms proposed for organo-mineral association in natural environment, ligand exchange, the displacement of surficial hydroxyl groups of minerals by organic functional groups, was considered a dominant and the strongest type of interaction, compared to cation bridging and van der Waals forces (Chorover and Amistadi, 2001; Gu et al., 1995). However, strong inner-sphere Fe-C covalent bond has been rarely examined at the organo-mineral interphase. Only a few studies were carried out in lab-manipulated and high ratio C to ferrihydrite systems, mainly using dissolved organic C (DOC), humic acids or aromatic ligands (Chen et al., 2016; Mikutta, 2011; Tamrat et al., 2019; Vantelon et al., 2019). Inner sphere Fe-C bonding were detected by XAS only at very higher C/(C+Fe) molar ratio ($\geq$0.71), suggesting substantial association between SRO Fe domains and DOC (Chen et al., 2016). Addition of aromatic hydroxybenzoic acid promoted organo-Fe(III) complexation. And increasing organo-Fe(III) complexes decreased ferrihydrite formation, especially in the coordination number (CN) of edge-sharing Fe and particle size (Mikutta, 2011). Natural aromatic organic C was proposed to trigger the formation of small ferrihydrite nanoparticles with increased structural strain, and enhance their biogeochemical reactivity in organic C-rich environment (Mikutta 2011). However, there was a vast difference in the spatial availability of

106　reactive functional groups or ligand among DOC, small-ring aromatic ligands and BC, in terms of

107　binding with ferrihydrite (Mikutta, 2011; Vantelon et al., 2019; Wen et al., 2019). No systematic

108　investigations of organo-mineral association and interacting mechanism between BC and SRO

109　minerals (especially ferrihydrite) in natural samples has been reported.　We aim to investigate how

110　BC enriches SRO minerals in the natural environment and probe the interphase organo-mineral

111　interaction by using synchrotron-based microscopic and spectroscopic techniques. The speciation of

112　Fe-minerals, in-situ distribution of BC functional groups and the possible interplay bond between BC

113　and associated SRO minerals were explored for a mechanistic understanding.

114

115　**2.　MATERIALS and METHODS**

116　**2.1.　Sample information and background**

117　　Black C-rich Amazonian Dark Earth (ADE, Anthrosols) and adjacent soils (Oxisol) with similar

118　mineralogy (Liang et al., 2006) were sampled from site Hatahara (HAT), near Manaus, Brazil (3°8'S,

119　59°52'W, 40–50 m above the sea level). The ADE (locally known as 'Terra Preta de Indio') are the

120　anthropogenic result of pre-Columbian settlements, developed on Oxisols and Ultisols. The age of

121　organic C has been estimated to range from 600–1000 years BP at HAT (Neves et al., 2003). Samples

122　were taken from a sub-horizon (43-69 cm depth) and air-dried. Detailed soil properties were included

123　in Liang et al. (2006). Particulate BC were hand-picked from ADE for in-situ analysis (TXM, X-ray

124　Micro-diffraction and FPA-FTIR), and in which primary texture such tracheid, pit and vascular can

125　be recognized under optical microscopy. The ADE sample for bulk analysis includes particulate BC,

126　amorphous BC and soil minerals.

127

128　**2.2. X-ray diffraction for mineralogy**

129　　To analyze the mineralogy, powder sample ADE, particulate BC and adjacent soil, were ground

130　and injected into capillary tubes (Special Glass 10, Hampton Research, CA) for synchrotron-based

131　X-ray diffraction analysis at the 09A beamline of Taiwan Photon Source (TPS), which was equipped

132　with a set of high-resolution monochromator (HRM). The wavelength was 0.82656 Å at the energy

133　of 15 keV. The X-ray diffraction (XRD) spectra were recorded under room temperature for 60 s

134　accumulation time. Specific X-ray diffraction peaks and patterns were assigned ICDD using the PDF-

135　2/4 program.

136

137　**2.3. Poorly crystalline Al/Fe extraction using ammonium oxalate**

138　Soil was freeze dried under vacuum and extracted using 30 ml of 0.2 M ammonium oxalate at

139　pH 3 for 0.5 g of sample, following the method by Drees and Ulery (2008), which were adapted from

140　USDA Soil Survey Laboratory Methods Manual.

141　The samples were incubated on a rotator in the dark for 4 hours, and then centrifuged at 3000

142　rpm for 5 minutes. The supernatant was collected to analyze Al and Fe after filtration through 0.22

143　μm. The content of Al and Fe ions were measured by inductively coupled plasma optical emission

144　spectrometry (ICP-OES) (iCAP, Thermo-Fisher Scientific).

145

146　**2.4. Elemental mapping by SEM-EDS**

147　For correlated spatial distribution of selected elements (C, O, Fe, Al, Si etc.) in BC particles

148　from ADE, a low-vacuum scanning electron microscope (JEOL W-LVSEM, JSM-6360LV) equipped

149　with an energy dispersive X-ray spectrometer (Oxford EDS) was used for elemental mapping, at an

150　accelerating voltage of 15 KeV.

151

152　**2.5. Sample preparation for in-situ analyses of TXM, FPA-FTIR and X-ray micro-**

153　　**diffraction**

154　Thin section for particulate BC samples were prepared with PELCO® Quickstick 135 (TED

155　PELLA, INC.). The sample subsequently hand-polished to a thickness of 30-50 μm for TXM and 10-

156 20 μm for FTIR. For TXM observation, each section was transferred onto Kapton tape and mounted

157 on a stainless steel sample holder. Before TXM analysis, gold nanoparticles (50-150 nm) were

158 deployed on the section surface for image registration. For FTIR analysis, the polished samples were

159 immersed in acetone overnight to remove the embedding materials.

160   The synchrotron-based Transmission X-ray Microscope (TXM) at TLS BL01B (NSRRC) is a

161 well-established technique for high spatial resolution 3-D tomography on fine samples. It is a powerful

162 tool for probing organo-mineral in-situ interaction and spatial distribution in environmental samples. Being

163 a non-destructive probe, it was successfully applied for organo-mineral *in situ* investigation of BC

164 structural network and submicron mineral morphology and spatial distribution (Weng et al., 2018). A

165 superconducting wavelength shifter source conducts a photon flux of 4×10^{11} photons s^{-1} (0.1% bw)$^{-1}$

166 in the energy range of 5-20 keV at the BL01B1 beamline. A double crystal monochromator exploiting

167 a pair of Ge (111) crystals selects X-rays within the energy range of 8-11 keV. The specimen was

168 imaged using a Fresnel zone plate, which functions as an objective lens for an image magnification

169 of 44× by the first order diffraction mode. Conjugated with a 20× downstream optical magnification,

170 the TXM provides a total magnification of 880×, and the field of view is 15×15 μm^2. By acquiring a

171 series of 2D images with the sample rotated 1° stepwise, 3-D tomography datasets are later

172 reconstructed based on 171 sequential image frames that are captured with azimuth angle rotating

173 from -85° to +85°. Under the most frequently used absorption-contrast mode, 2-D images are recorded

174 based on the projection of different X-ray absorption coefficient integration along the optical pathway.

175 Three-dimensional tomography reconstruction was performed using homemade software, which was

176 coded based on iterative image registration (Faproma) (Wang et al., 2017) and filtered back projection

177 (FBP) reconstruction algorithms. The exported cross-section of 3-D tomography (reconstructed

178 datasets) showed the real distribution details and boundary interplay of BC and minerals. The

179 reconstructed datasets were exported in cross-sections for 3-D tomographic structures visualization

180 and illustration using *Amira*. The intensity contrast of reconstructed datasets was inversed for better

181 visualization. Compositions with higher absorption coefficients were shown in higher intensity and

182 those with low absorption coefficients were shown in lower intensity.

183

2.6. FTIR microspectroscopy

185   For bulk sample FTIR analysis, soil and BC powder samples were first dried at 60 °C overnight,

186 then mixed ratios of BC sample and potassium bromide (KBr), such as 1:100 (0.001g sample and

187 0.1g KBr), were molded into transparent disks using a hydraulic press. During the press period, a

188 vacuum pump was used for evacuating air and water.

189   Carbon functional groups and mineral features were fingerprinted at beamline BL14A1

190 infrared microspectroscopy (IMS) end-station of NSRRC, Taiwan Light Source (TLS), which

191 includes a FTIR spectrometer (Nicolet 6700, Thermo Fisher Scientific, Madison, WI, USA) for

192 bulk samples and a confocal infrared microscope (Nicolet Continuum; Thermo Fisher Scientific,

193 Madison, WI, USA) for imaging. The FPA-FTIR system was equipped with a FTIR spectrometer

194 (IFS 66 v/S, Bruker, Ettlingen, Germany), an IR microscope (Hypersion 3000, Bruker, Ettlingen,

195 Germany), and a LN-cooled 64×64 pixels MCT FPA detector (Santa Barbara Focal plane, Goleta,

196 CA, USA). The BC thin sections were imaged by a 32× Casse grain objective. A Self-equipped

197 light source was directed to focus on a $10 \times 10 \ \mu m^2$ infrared spot, and the lateral mapping step size

198 was set at 10 μm. In order to achieve a high signal/noise (S/N) ratio, measurement was conducted

199 over a $50 \times 30 \ \mu m^2$ infrared spot using a conventional global infrared source. The scan number was

200 increased to enhance the signal-to-noise ratio. A total of 1024 scans was performed for point analysis

201 within the range of 4000 to 450 cm^{-1} at a resolution of 4 cm^{-1}. For FPA, 256 scans were performed

202 within the range of 4000 to 550 cm^{-1}. The optical path was continuously purged using liquid nitrogen.

203 The FPA-FTIR spectral images were computed by integrating characteristic infrared absorbance

204 for different carbon forms in the range of 1625-1595 cm^{-1} for aromatic C-H, 1730-1650 cm^{-1} for

205 carbonyl and carboxylic C=O, and 3750-3550 cm^{-1} for lattice water O-H in clay minerals. The

206 automatic atmospheric suppression function in OMNIC (OMNIC 9.2, 2012; Thermo Fisher

207 Scientific Inc., Waltham, MA, USA) for bulk BC analysis and in OPUS (OPUS 7.2, 2012; Bruker,

208 Ettlingen, Germany) for BC thin-sections was activated during the data analysis to eliminate the

209 rovibration absorptions of CO_2 and water vapor in ambient air.

210

2.7. X-ray micro-diffraction and fluorescence mapping

212 Spatially resolved characterization of different minerals within heterogeneous samples can be

213 achieved by X-ray micro-diffraction. We first explored the nature of BC-mineral complexes using

214 Laue X-ray Nano-diffraction (XND) at TPS beamline 21A (NSRRC) for fast mapping of

215 polycrystalline samples. X-ray micro-diffraction data were collected in transmission geometry at

216 beamline 12.3.2 of the Advanced Light Source (ALS) at an energy of 10 keV, using a DECTRIS

217 Pilatus 1M detector placed at an angle of 39 degrees and a distance of 158 mm from the sample

218 (Tamura et al., 2009) . X-ray microfluorescence data were collected using a Vortex EM silicon-drift

219 detector. Experimental geometry calibration was obtained through calibration on an alumina powder.

220 Data analysis was performed using the X-Ray Micro-diffraction Analysis Software (XMAS)

221 (Tamura, 2014).

222

2.8. Iron K-edge X-ray absorption spectroscopy (XAS)

224 The species and chemistry coordination of Fe in ADE, BC and adjacent soil was characterized

225 using XAS at beamline 16A1 and 17C1 at NSRRC, Taiwan Light Source (TLS). Air-dried soil

226 samples and particulate BC were grounded and mounted on scotch tape. In order to enhance the S/N

227 ratio of spectra, multiple layers of samples were applied. A reference of Fe metal foil was used for

228 Fe K-edge energy calibration at 7112.0 eV before sample analyses. The XAS spectra were collected

229 at room temperature in the fluorescence mode using a Ar(g)-filled Lytle detector and a Si (111)

230 monochromator. The XAS spectra were recorded 190 eV below and 1000 eV above 7112 eV using a

231 step size of 4 eV for pre-edge (-190 to -10 eV), a step size of 0.35 eV for near-edge (-10 to +30 eV)

232 and a step size of 0.05 eV for post-edge (+30 to +1000 eV). In order to improve the S/N ratio, multi-

233 scans were applied (4 times for adjacent soil, 9 times for ADE and 21 times for BC) and the spectra

234 were aligned, merged and processed using the IFEFFIT interface including Athena and Artemis

235 programs (version 1.2.11, Matthew Newville, The University of Chicago). The reference materials

236 used included goethite, hematite, and ferrihydrite. For extended X-ray absorption fine structure

237 (EXAFS) fitting, theoretical scattering paths were calculated with FEFF6 using the structural model

238 of two-line ferrihydrite (Michel et al., 2007; Zabinsky et al., 1995). The fitting model represented all

239 single scattering (SS) Fe-O, and Fe-Fe paths out to a maximum radial distance of 3.5 Å. All EXAFS

240 spectra were fit for coordination number (CN), distance (ΔR), and mean-square displacement of

241 interatomic distance (σ^2) with a fixed amplitude reduction factor (S_0^2) of 0.83 derived from the first-

242 shell fitting of hematite (Liu and Hesterberg, 2011). Paths in the model designated as Fe-Fe[1] and Fe-

243 Fe[2] represented the interatomic distances of edge-sharing (ES) and corner-sharing (CS) FeO_6 linkages

244 in the two-line ferrihydrite structure (Manceau and Drits, 1993). A path with Fe-C was also tried to

245 replace Fe-Fe[1] for EXAFS spectra fitting.

246

3. RESULTS

3.1. Mineralogy of ADE, BC and adjacent Soil

249 Based on the XRD patterns, the mineralogy of ADE and BC is similar to the adjacent soil (Fig.

250 1A). Quartz (PDF_00-033-1161) is the most dominant crystalline mineral phase. The other major

251 mineral phases are aluminosilicates, such as kaolinite (PDF_01-078-1996) and anorthite (PDF_00-

252 0141-1486). The major crystalline Fe-minerals in crystal phases included hematite (PDF_00-033-

253 0664) and goethite (PDF_01-075-5065), and ferrihydrite (PDF_01-073-8408) were also identified.

254 Diagnostic peaks of kaolinite and quartz were found in FTIR spectra of BC, ADE and adjacent soil

255 (Table S1) (Parikh et al., 2014). Bands of OH deformation of inner surface hydroxyl groups in

256 kaolinite were observed at 937 cm^{-1} and 910 cm^{-1} (Vaculikova et al., 2011).

257

3.2. Enrichment of SRO Fe-Minerals and amorphous phases in BC and ADE

The concentration of SRO minerals in BC-rich ADE by ammonium oxalate extraction was 47.34 ppm for Al and 42.98 ppm for Fe, respectively, which was 100% higher than that in adjacent soil (Fig. 1B).

Based on X-ray diffraction, difference in crystal phase was found mainly in the fractions of crystalline Fe-minerals including hematite and goethite, as well as SRO ferrihydrite. The peak for ferrihydrite was very broad. Linear combination fitting (LCF) of k-spacing in EXAFS revealed the composition of Fe-minerals, and there were 59.8% of ferrihydrite, 20.3% of hematite and 19.9% of goethite in ADE sample (Table 1; Fig. S1). In contrast, there were 58.3% of ferrihydrite and 41.7% of goethite in the adjacent soil. Whereas, up to 81.1% of ferrihydrite and 18.9% of hematite were identified in BC. The Fe-minerals in association with BC were mainly SRO ferrihydrite and some amorphous Fe-phases (Table 1, Table 2). Overall, SRO ferrihydrite and amorphous Fe-phases are more abundant in ADE than in the adjacent soil. Among the poorly crystalline phases, ferrihydrite was highly enriched in BC particles.

3.3. Intimate spatial correlation between BC and minerals revealed by SEM-EDS

According to SEM-EDS elemental mapping, the minerals coating on BC are mainly aluminosilicates (kaolinite), Fe-minerals and Ca-rich minerals (Fig. 2). Spatially, Al and Si distributed mostly on the peripheral region of BC structure. Iron followed a similar spatial pattern, yet was of much lower intensity and abundance. The distribution of Ca was highly correlated to C. The co-localization of Al, Si, Fe, Ca and C revealed an intimate spatial correlation between BC and minerals in ADE.

3.4. In-situ observation of poorly crystalline minerals at the organo-mineral Interface

The exported 3-D tomography images revealed the in-situ spatial distribution of BC (in grey) and

283　non-uniform coating of microcrystal and nanocrystal minerals (in rouge) on BC at the submicron scale

284　(Fig. 3). The plant vascular structure preserved in BC provided substantial surface sites for minerals

285　absorption and precipitation (Fig. 3A). Abundant submicron minerals particles were observed coating on

286　BC surface, in clusters, sheets and layers (Fig. 3 B, D, E). Morphologically, the minerals were anhedral or

287　subhedral, and lack of the distinct morphological feature of developed crystals (Zbik et al., 2010) (Fig.

288　3B). Anhedral and subhedral minerals are often poorly crystalline.

289　　　High resolution X-ray fluorescence maps revealed the heterogeneous composition distribution

290　of mineral on BC, including Fe- and Ca- minerals (Fig. 4A, B). Incomplete shielding by nano-

291　minerals was observed in the interphase region between BC and minerals, and the overall mineral

292　density varied from regions to regions (Fig. 4 D, E, F). The minerals detected by X-ray powder

293　diffraction were kaolinite and goethite. Micro-diffraction analyses revealed that the texture of clay

294　minerals was nano-crystalline kaolinite, and the goethite was micro-crystalline in the Fe hot spot (Fig.

295　4C). No signal of poorly crystalline ferrihydrite was captured by micro-diffraction, due to their low

296　degree of crystallinity and small size, which was less than the probe.

297

298　　**3.5. Organo-mineral association**

299　　　For typical crystalline kaolinite, the ν(OH) bands show up at 3695, 3668, 3651, and 3620 cm^{-1}

300　(Madejová, 2003) . Only three OH stretching vibrations were observed at 3698, 3652, and 3621 cm^{-1}

301　in ADE and the adjacent soil, pointing to the poorly crystalline nature of kaolinite (Fig. 5A). The peak

302　for enhanced absorption was broader at 3652 cm^{-1} in BC, compared to ADE and adjacent soil,

303　revealing a lower level of crystallinity. The kaolinite in ADE was more dickite-like and poorly

304　crystalline, compared to adjacent soil (Fig. 5A). The peak ratio of 1034 cm^{-1} to 3698 cm^{-1} was lower

305　in BC, compared to ADE and adjacent soil, pointing to a lower crystallinity and involvement of clay

306　minerals in BC (Fig. 5B, C, D, E). The core of BC was mainly aromatic (C=C, 1604 cm^{-1} within

307　1625-1595 cm^{-1}, Fig. 5C), and the distribution of reactive functional groups (1650-1730 cm^{-1}, Fig.

308　5D) including carbonyl (C=O, 1666 cm^{-1}, in conjunction with aromatic ring) and carboxyl groups

309 (C=OOH, 1715 cm^{-1}) were mostly on the peripheral region of aromatic C (Sharma et al., 2010). The

310 distribution of clay minerals (lattice water O-H, 3550-3750 cm^{-1}) was by large correlated with the

311 presence of reactive functional groups on BC (Fig. 5E). However, there were regions where reactive

312 functional groups were enriched, whereas the signal of clay minerals was disproportionally low (Fig.

313 5 D, E). In these regions, Fe-minerals and Ca-minerals were in association with BC (Fig. 4A, B). The

314 broad and pronounced bands within 1200-1400 cm^{-1} and 1650-1730 cm^{-1} in BC suggested a

315 significant level of organo-mineral complexation (Kaiser et al., 2007). Strong signal of phenolic

316 functional groups (aryl-OH) were observed at 1241 cm^{-1} (Özçimen and Ersoy-Meriçboyu, 2010;

317 Parikh et al., 2014). Band at 1380-1384 cm^{-1}was identified to denote inner sphere complexation of

318 Fe and aromatic C (Fu and Xuan, 2006; Sowers et al., 2018).

319

320 **3.6. Chemical coordination of SRO Fe-mineral in interplay with BC**

321 For the chemical coordination of Fe-minerals, the Fe-O path was first fitted with the hematite

322 structure which was octahedral, and the coordination number (CN) was fixed at 6. Our fitting result

323 revealed that the CN of the first shell Fe-Fe^1 was higher in BC (2.36±0.51), compared to ADE (1.68

324 ±0.56) (Table 2, Fig. S2). The second shell Fe-Fe^2 fitting result followed a similar trend and a higher

325 CN was found in BC (1.30±0.65), compared to ADE (0.47±0.40). A higher CN in BC denoted a

326 higher degree of order in coordination between neighboring Fe mineral crystals, resulting from SRO

327 mineral enrichment. The bonding length properties were similar for the first and second shell of Fe-

328 Fe in BC (2.98±0.01, 3.41±0.04 Å) and ADE (2.98±0.02 Å, 3.38±0.06 Å). The bonding length of

329 the first (Fe-Fe^1) shell was short and overlapped the range of Fe-C bond (2.95-2.99 Å). However, no

330 Fe-C path was not successfully fitted in BC after placing the first (Fe-Fe^1) path. Compared to adjacent

331 soil (3.00±0.01 Å), a downshift of the first (Fe-Fe^1) shell was observed in BC (2.98±0.01 Å).

332 Compared to ADE, a higher intensity of Fe-Fe^1 and Fe-Fe^2 oscillation was found in the adjacent soil,

which had a higher portion of goethite. No significant difference in the bonding length were found between ADE and adjacent soil. A small but distinct peak was observed at 5.7 Å^{-1} in the EXAFS k oscillation of BC, which was characteristic of Fe-O-C bonds. A very weak shoulder at 5 Å^{-1}, a strong peak at 7.5 Å^{-1}, and a weak peak at 9.5 Å^{-1} were also observed in BC, pointing to the presence of ferrihydrite (Fig. S3).

4. DISCUSSION

4.1. Dynamic neoformation of SRO minerals by biogeochemical cycling

According to 3-D tomography, the physical protection of BC was attributed to submicron minerals, including nano-crystalline kaolinite and poorly-crystalline Fe-minerals, which had no specific crystal morphology and often appeared as clusters and envelope-like structures (Fig. 3). The mineral sheet stacking on BC surface was a unique characteristic of BC-mineral complex and its layer thickness, density and uniformity might be regulated by multiple abiotic environmental factors including pH and availability of cations and anions (Fig. 3E). The subhedral or anhedral morphology revealed their susceptibility to weathering and transformation.

The high leaching and weathering environment in the tropics often accelerate the chemical weathering of silicates minerals including clays and feldspars, resulting in dynamic output of ionic compounds and formation of amorphous compounds (e.g. Fe octahedra) (Mikutta et al., 2005). And amorphous compounds prone to transform to SRO minerals (e.g. ferrihydrite, and allophane) and further to crystalline Fe-minerals (e.g. hematite and goethite) (Fig. 6) and Al-mineral gibbsite (Rasmussen et al., 2005). In the lab studies, though organic C, solution impurity or cations could delay the transformation of ferrihydrite to hematite or goethite, the conversions would still occur within a few years (Schwertmann and Murad, 1983). In the case of SRO ferrihydrite enrichment in ADE, it was inferred that the reactive functional groups on BC surface hindered the transformation of ferrihydrite to hematite or goethite, thus ferrihydrite could be stabilized for an extended period of time (Mikutta, 2011). The extraordinary enrichment of ferrihydrite up to 81.1% in the more than 600

359 years old BC, suggested not only a delayed transformation, but also a dynamic and ongoing

360 neoformation of SRO minerals in a redox-fluctuating environment (Fig. 6) (Liang et al., 2006; Hall

361 et al., 2016).

362   The frequent forest fires, flooding and drainage in Amazon Basin could generate Fe (oxy-hydro)

363 oxides by thermal transformation or phase transformation in aqueous conditions (Das et al., 2011;

364 Jiang et al., 2018; Schwertmann and Murad, 1983). We ruled out the pyrogenic path of forming SRO

365 ferrihydrite in BC, as no meta-kaolinite and shift of 001 reflections were observed. On the other hand,

366 ferrihydrite and goethite could be transformed into hematite at a temperature above 250-300℃, so

367 even a small fire could convert most Fe-minerals to a hematite (Bailey and Anderson, 1980; Gualtieri

368 and Venturelli, 1999; Saito et al., 2016). We concluded that the neoformation of ferrihydrite was a

369 result of biogeochemical cycling from the dynamic equilibriums of amorphous compounds in ADE.

370

371 **4.2. SRO ferrihydrite transformation controlled by pH microenvironment**

372   In the long-term perspective, SRO ferrihydrite (poorly crystalline Fe(III) hydroxide) is a

373 metastable phase (Das et al., 2011) and tends to transform into more crystalline or long-range-order

374 (LRO) mineral/Fe(III) oxides, such as hematite at neutral pH (around 7) and goethite at low (2-5) or

375 high (10-14) pH (Fig. 6) (Schwertmann and Murad, 1983). Dependent on the pH microenvironment,

376 crystalline hematite or goethite are formed either through a dissolution-crystallization process or in

377 the solid state through a topotactic transformation (Cudennec and Lecerf, 2006; Schwertmann and

378 Cornell, 2000). According to the batch experiments by Schwertmann and Murad (1983), goethite was

379 mainly formed in pH either below 5 or higher than 9. In BC, the associated Fe-minerals were mainly

380 ferrihydrite and hematite. In ADE, there was only a small fraction of goethite (19.9%) (Fig. 1; Table

381 1). Thus a local pH of 5~9 in ADE and BC was constrained. If this pH index was further applied to

382 the adjacent soil, the pH was constrained to fall within the range of 3~5. Our prediction based on Fe-

383 mineral speciation matched well with the measured values, which were between 5.5-6.4 in bulk ADE

384 and 3.8-4.6 in the adjacent soil (Liang et al., 2006). Our research supported that the transformation of

385 ferrihydrite in ADE were controlled by the local pH environment.

386

387 **4.3. Black C enriched SRO minerals in ADE**

388 The concentration of poorly crystalline Fe-minerals was 100% higher in ADE than that in

389 adjacent soils, showing an enrichment of SRO minerals in the BC-rich ADE (Fig. 1). The

390 considerable enrichment of ferrihydrite up to 81.1% in BC suggested a unique accumulation and

391 stabilization of reactive minerals by interacting with functionalized aromatic C in a high-leaching

392 environment. When the unique and high affinity between ferrihydrite and aromatic C was concerned,

393 other experiments revealed that the ferrihydrite-associated material was enriched in aromatic

394 components (Eusterhues et al., 2011). Within the pH range of 4.5-6.5, the net surface charge of SRO

395 ferrihydrite is positive, which readily facilitates forming of strong covalent bonds between SRO

396 ferrihydrite and the negatively charged BC surface (Hiemstra and Van Riemsdijk, 2009). The EXAFS

397 fitting showed that the CN in both edge-sharing and corner-sharing Fe-Fe coordination was higher in

398 BC than that in ADE (Table 2). A higher CN in BC denoted a higher degree of order in coordination

399 between neighboring Fe mineral crystals, resulting from SRO ferrihydrite enrichment instead of

400 clustering of FeO_6 octrahedra or Fe oligomers (Vantelon et al., 2019). Based on the LCF result,

401 ferrihydrite accounted for only 51.5% and 53.2% of the Fe-phases in ADE and the adjacent soil. It

402 suggested that the higher CN in BC were not due to the presence of other Fe-phases other than SRO

403 ferrihydrite. The lower CN of Fe-Fe coordination in ADE illustrated that the major Fe-phases derived

404 from severe weathering process are more amorphous compared to BC. There was likely a higher

405 fraction of corner sharing FeO_6 octahedra in ADE, which was locked up by soil labile C (including

406 DOC and humic acids) via organo-Fe complexation (Liang et al., 2010). On BC surface, the

407 amorphous Fe-phases were retained by strong organo-mineral association and their progressive aging

408 was down-tuned. The clustering of FeO_6 octahedra transformed to SRO ferrihydrite (Fig. 6). With

409 the ongoing neoformation of SRO minerals via biogeochemical cycling, the reactive surface of BC

410   provided abundant association sites for adsorption of neo SRO ferrihydrite and resulted in subsequent

411   enrichment. As for the adjacent soil, a typical tropical soil, the local Fe coordination was explained

412   by the dominant phases including goethite and ferrihydrite.

413

4.4. The mechanism for organo-mineral interaction

415   Various reactive functional groups including phenolic (aryl-OH) and carbonyl (-COO; 1650-

416   1730 cm^{-1}) were identified on BC surface (Fig. 5; Liang et al., 2006). The net surface charge of SRO

417   ferrihydrite is positive within the pH range of ADE and BC (Hiemstra and Van Riemsdijk, 2009).

418   Strong covalent bond was identified between SRO ferrihydrite and negatively charged BC. The FTIR

419   Band at 1380-1384 cm^{-1} revealed inner sphere complexation of Fe and aromatic C with reactive

420   functional groups (Fig. 5; Table S1) (Fu and Xuan, 2006; Sowers et al., 2018). In terms of chemical

421   affinity, the broad and pronounced FTIR band at 1241 cm^{-1} (aryl-OH) denoted a significant level of

422   organo-mineral complexation between BC and poorly crystalline minerals (Kaiser et al., 2007;

423   Özçimen and Ersoy-Meriçboyu, 2010; Parikh et al., 2014). In BC, the small but distinct peak observed

424   at 5.7 Å^{-1} in the EXAFS k oscillation was characteristic of Fe-O-C bonds (Tamrat et al., 2019).

425   However, the XAS analyses of Fe-Fe coordination failed to identify the Fe-C covalent bond in BC

426   when a peak downshift was observed. Though no Fe-C or Fe-O-C path was successfully fitted, the

427   bonding length of the first (Fe-Fe[1]) shell in BC was short (2.98±0.01 Å) and largely overlapped the

428   range of Fe-C bond (2.95-2.99 Å), suggesting two nearby paths are excluding each other (Chen et al.,

429   2016).

430   Organic C strongly interfered with ferrihydrite crystal growth, leading to smaller crystal,

431   increased lattice spacings and more distorted FeO$_6$ octahedra or Fe oligomers (Chen et al., 2016;

432   Mikutta, 2011; Vantelon et al., 2019). Even a small amounts of DOC can significantly change the

433   particle size and structural order of ferrihydrite (Eusterhues et al., 2008). The degree of order in

434   precipitated SRO ferrihydrite decreased when the ratio of C to Fe increased, and the Fe-Fe

435 coordination shifted from edge-sharing to corner-sharing (Chen et al., 2016). The Fe-C path was

436 successfully fitted only when the ratio of C to Fe was high (Chen et al., 2016; Mikutta, 2011). No Fe-

437 C path was fitted at a (C/C+Fe) molar ratio below 0.62. In contrast, the first Fe-Fe[1] shell would not

438 fitted at a high (C/C+Fe) ratio at 0.89 at pH 4.5 (Chen et al., 2016). The low fitting abilities of Fe-C

439 or Fe-O-C in BC and ADE revealed a mixture of multiphase Fe-compound in the samples, in which

440 SRO ferrihydrite was the most reactive and dominant phase. The unsuccessful fitting of Fe-C bond

441 could imply:1) the (C/C+Fe) ratio was likely lower than 0.62, and 2) the availability of Fe-C covalent

442 bonds were less abundant than in the high C to Fe co-precipitation system. We argued that the

443 (C/C+Fe) ratios which were tested in the DOC system would not readily apply to BC, as there was

444 vast difference in the spatial availability and conformation of reactive functional groups or ligands

445 between DOC and BC, and only a limited portion of C on BC surface were involved in the organo-

446 mineral interaction. The very weak shoulder at 5~5.2 $Å^{-1}$, strong peak at 7.5 $Å^{-1}$ and weak peak at 9.5

447 $Å^{-1}$ in the EXAFS k oscillation spectra, suggesting the presence of SRO ferrihydrite instead of corner-

448 sharing FeO_6 octahedra (Fig. S3) (Mikutta, 2011; Tamrat et al., 2019). We rationaled that the

449 availability of inner-sphere Fe-C complexation was limited to BC surface and interphase region. The

450 negatively charged reactive functional groups on BC surface interplayed with the positively charged

451 SRO ferrihydrite through strong covalent bond, thus limited the progressive aging of poorly

452 crystalline Fe phases towards better crystallized and more stable Fe oxides, and explained enrichment

453 of SRO ferrihydrite in BC.

454 Besides strong covalent bond, aromatic C could be selectively sorbed by Fe-minerals via other

455 weaker types of binding included ligand exchange and cation bridging (Fig. 6) (Mikutta et al., 2007;

456 Mikutta and Kaiser, 2011; Chorover and Amistadi, 2001). Iron (III) can act as a strong bridging cation,

457 and Fe-minerals are effective ligands (Ahmed et al., 2002; Gu et al., 1995). The operating binding

458 mechanisms and subsequent desorption and availability of organic C depend on soil solution

459 chemistry and the (surface) type of minerals (Mikutta et al., 2007). Different bonding strength was

460 modulated by specific aromatic-C conformations (Hernes et al., 2013; Mikutta, 2011). The

microcrystalline goethite found in the Fe hot spot in BC might only play a negligible role in organo-mineral interaction.

The EDS mapping and micro-XRF mapping illustrated a high spatial correlation between Ca and C. Calcium could serve as a strong cation bridging agent between BC surface and nano-crystalline kaolinite clay mineral, which were both negatively charged (Fig. 6). Calcium bridging enhanced the stability of sorbed organic C, though to a less extent when compared to the binding via 'ligand exchange' (Mikutta et al., 2007; Chorover and Amistadi, 2001). Besides acting as a base cation, Ca^{2+} can readily exchange its hydration shell and create inner sphere complexes with organic functional groups (Roïnkens and Dolfing, 1998). Both inner- and out-sphere bridging by Ca^{2+} may play an active role in the stabilization of organic C in soil (Rowley et al., 2018). The neoformation of other minerals involving Ca, Si etc and their interaction with BC were not explored or discussed here (Tamrat et al., 2019).

The reaction of organic ligands with Al^{3+} and sorption to amorphous Al compounds or SRO Al-minerals was strongly correlated with the storage and long-term stabilization of soil organic C (Masiello et al., 2004; Percival et al., 2000; Rasmussen et al., 2005). Chemical stabilization of organic C was considered a key process controlling soil C accumulation, whereas clay content was only poorly related to long-term C stabilization. The interplay mechanism between BC and SRO Al-minerals warrants further studies.

4.5. Environmental Implications

Our findings put forward a strong appeal that the complex interplay between BC aging-driven surface modifications and SRO mineral may play an important role on the long-term stabilization of BC. Our research argued that the interactive chemistry of BC and associated minerals and their physical presence were both important for the long-term stabilization of organic C. The enrichment of poorly crystalline minerals could have a positive feedback on the long-term stabilization of BC and warrants future research. The scale up application of biochar into agri- and ecological system may have a long

lasting impact on the transformation of associated minerals. Considering the vast difference between lab setup and field conditions, we suggest that future studies on the organo-mineral mechanisms should take the diversity of natural BC samples and field conditions into account.

Fresh biochar may alter the pH microenvironment in soil and render mineral transformation. The clay mineral kaolinite may have a higher potential for organo-mineral interplay and cation adsorption due to its nano-crystalline feature in tropical Amazon.

5. CONCLUSION

This study characterized BC and associated poorly crystalline minerals at fine scale, and probed the mechanisms of organo-mineral interaction. Synchrotron-based 3-D tomography generated high spatial resolution images and illustrated the in-situ distribution of BC and submicron poorly crystalline minerals at the interphase. Abundant minerals nanoparticles were observed on BC surface, in clusters and layers, pointing to a high level of physical protection. Ferrihydrite contributed up to 81.1% of Fe-minerals in BC. Black C limited the progressive aging of poorly crystalline Fe phases and enriched SRO ferrihydrite to a great extent in a redox fluctuating and high-leaching environment. The degree of order in coordination between neighboring Fe mineral crystals was higher in BC due to SRO ferrihydrite enrichment. The characteristic Fe-O-C bond was observed at 5.7 $Å^{-1}$ in the EXAFS k oscillation of BC. No Fe-C path (or Fe-O-C bond) was successfully fitted by XAS analyses for Fe coordination, suggesting the availability of inner-sphere Fe-C complexation was limited to BC surface and interphase region. The main minerals on BC via organo-mineral complexation was SRO ferrihydrite instead of corner-sharing FeO_6 octahedra or Fe oligomers. Our research revealed that the transformation of SRO ferrihydrite to more crystalline Fe oxides were controlled by the local pH environment in ADE and adjacent soil. There was a significant level of organo-mineral complexation and band of inner sphere Fe-aromatic C complexation was identified by FTIR. The negatively charged reactive functional groups on BC surface interacted with positively charged SRO ferrihydrite through covalent bond, ligand exchange and cation bridging.

Competing financial interests

The authors declare no competing financial interests.

REFERENCES

Ahmed N., Varadachari C. and Ghosh K. (2002) Soil clay–humus complexes. II. Bridging cations and DTA studies. *Soil Res.* **40**, 705-713.

Bailey A.W. and Anderson M.L. (1980) Fire temperatures in grass, shrub and aspen forest communities of Central Alberta. *Rangeland Ecology & Management/Journal of Range Management Archives* **33**, 37-40.

Brodowski S., Amelung W., Haumaier L., Abetz C. and Zech W. (2005) Morphological and chemical properties of black carbon in physical soil fractions as revealed by scanning electron microscopy and energy-dispersive X-ray spectroscopy. *Geoderma* **128**, 116-129.

Chen C., Dynes J.J., Wang J., Karunakaran C. and Sparks D.L. (2014a) Soft X-ray spectromicroscopy study of mineral-organic matter associations in pasture soil clay

539 fractions. *Environ. Sci. Technol.* **48**, 6678-6686.

540 Chen C., Dynes J.J., Wang J. and Sparks D.L. (2014b) Properties of Fe-organic matter associations

541 via coprecipitation versus adsorption. *Environ. Sci. Technol.* **48**, 13751-13759.

542 Chen K.-Y., Chen T.-Y., Chan Y.-T., Cheng C.-Y., Tzou Y.-M., Liu Y.-T. and Teah H.-Y. (2016)

543 Stabilization of natural organic matter by short-range-order iron hydroxides. *Environ. Sci.*

544 *Technol.* **50**, 12612-12620.

545 Chen Y., Zou C., Mastalerz M., Hu S., Gasaway C. and Tao X. (2015) Applications of micro-

546 fourier transform infrared spectroscopy (FTIR) in the geological sciences--A Review. *Int. J.*

547 *Mol. Sci.* **16**, 30223-30250.

548 Chia C.H., Gong B., Joseph S.D., Marjo C.E., Munroe P. and Rich A.M. (2012) Imaging of

549 mineral-enriched biochar by FTIR, Raman and SEM–EDX. *Vib. Spectrosc.* **62**, 248-257.

550 Cornell R.M. and Schwertmann U. (1996) The iron oxides : structure, properties, reactions,

551 occurrence, and uses. Weinheim : VCH.

552 Cudennec Y. and Lecerf A. (2006) The transformation of ferrihydrite into goethite or hematite,

553 revisited. *J. Solid State Chem.* **179**, 716-722.

554 Cusack D.F., Chadwick O.A., Hockaday W.C. and Vitousek P.M. (2012) Mineralogical controls on

555 soil black carbon preservation. *Global Biogeochem. Cy.* **26**, 2019.

556 Das S., Hendry M.J. and Essilfie-Dughan J. (2011) Transformation of two-line ferrihydrite to

557 goethite and hematite as a function of pH and temperature. *Environ. Sci. Technol.* **45**, 268-

558 275.

559 Drees L.R. and Ulery A.L. (2008) Methods of soil analysis. Soil Science Society of America.

560 Gualtieri A.F. and Venturelli P. (1999) In situ study of the goethite-hematite phase transformation

561 by real time synchrotron powder diffraction. *Am. Min.* **84**, 895-904.

562 Hiemstra T. and Van Riemsdijk W.H. (2009) A surface structural model for ferrihydrite I: Sites

563 related to primary charge, molar mass, and mass density. *Geochim. Cosmochim. Acta* **73**,

564 4423-4436.

565   Hockaday W.C., Grannas A.M., Kim S. and Hatcher P.G. (2006) Direct molecular evidence for the

566   degradation and mobility of black carbon in soils from ultrahigh-resolution mass spectral

567   analysis of dissolved organic matter from a fire-impacted forest soil. *Org. Geochem.* **37**,

568   501-510.

569   Jiang Z., Liu Q., Roberts A.P., Barrón V., Torrent J. and Zhang Q. (2018) A new model for

570   transformation of ferrihydrite to hematite in soils and sediments. *Geology* **46**, 987-990.

571   Kuhlbusch T.A. (1998) Black carbon and the carbon cycle. *Science* **280**, 1903-1904.

572   Liang B., Lehmann J., Solomon D., Kinyangi J., Grossman J., O'neill B., Skjemstad J., Thies J.,

573   Luizao F. and Petersen J. (2006) Black carbon increases cation exchange capacity in soils.

574   *Soil Sci Soc Am J.* **70**, 1719-1730.

575   Liang B., Lehmann J., Solomon D., Sohi S., Thies J.E., Skjemstad J.O., Luizao F.J., Engelhard

576   M.H., Neves E.G. and Wirick S. (2008) Stability of biomass-derived black carbon in soils.

577   *Geochim. Cosmochim. Acta* **72**, 6069-6078.

578   Liu Y.-T. and Hesterberg D. (2011) Phosphate bonding on noncrystalline Al/Fe-hydroxide

579   coprecipitates. *Environ. Sci. Technol.* **45**, 6283-6289.

580   Madejová J. (2003) FTIR techniques in clay mineral studies. *Vib. Spectrosc.* **31**, 1-10.

581   Manceau A. and Drits V. (1993) Local structure of ferrihydrite and feroxyhite by EXAFS

582   spectroscopy. *Clay miner.* **28**, 165-184.

583   Michel F.M., Ehm L., Antao S.M., Lee P.L., Chupas P.J., Liu G., Strongin D.R., Schoonen M.A.,

584   Phillips B.L. and Parise J.B. (2007) The structure of ferrihydrite, a nanocrystalline material.

585   *Science* **316**, 1726-1729.

586   Mikutta R. and Kaiser K. (2011) Organic matter bound to mineral surfaces: Resistance to chemical

587   and biological oxidation. *Soil Biol. Biochem.* **43**, 1738-1741.

588   Mikutta R., Mikutta C., Kalbitz K., Scheel T., Kaiser K. and Jahn R. (2007) Biodegradation of

589   forest floor organic matter bound to minerals via different binding mechanisms. *Geochim.*

590   *Cosmochim. Acta* **71**, 2569-2590.

591 Neves E.G., Petersen J.B., Bartone R.N. and Da Silva C.A. (2003) Historical and socio-cultural

592   origins of Amazonian dark earth, Amazonian dark earths. Springer, pp. 29-50.

593 Parikh S.J., Goyne K.W., Margenot A.J., Mukome F.N.D. and Calderón F.J. (2014) Soil chemical

594   insights provided through vibrational spectroscopy, pp. 1-148.

595 Ramanathan V. and Carmichael G. (2008) Global and regional climate changes due to black carbon.

596   *Nat. Geosci.* **1**, 221.

597 Rocha J. and Klinowski J. (1990) Si-29 and Al-27 Magic-angle-spinning NMR-studies of the

598   thermal transformation of kaolinite. *Phys. Chem. Miner.* **17**, 179-186.

599 Saito G., Nomura T., Sakaguchi N. and Akiyama T. (2016) Optimization of the dehydration

600   temperature of goethite to control pore morphology. *ISIJ Int.* **56**, 1598-1605.

601 Schmidt M.W. (2004) Biogeochemistry: Carbon budget in the black. *Nature* **427**, 305.

602 Schwertmann U. and Cornell R. (2000) The laboratory synthesis of Iron Oxides. Wiley-VCH:

603   Weinheim.

604 Schwertmann U. and Murad E. (1983) Effect of pH on the formation of goethite and hematite from

605   ferrihydrite. *Clay Clay Miner.* **31**, 277-284.

606 Singh B., Fang Y. and Johnston C.T. (2016) A Fourier-transform infrared study of biochar aging in

607   soils. *Soil. Sci. Soc. Am. J.* **80**, 613-622.

608 Tamura N. (2014) XMAS: A versatile tool for analyzing synchrotron X-ray microdiffraction data,

609   Strain and dislocation gradients from diffraction: Spatially-Resolved Local Structure and

610   Defects. World Scientific, pp. 125-155.

611 Tamura N., Kunz M., Chen K., Celestre R., MacDowell A. and Warwick T. (2009) A superbend X-

612   ray microdiffraction beamline at the advanced light source. *Mater. Sci. Eng. A* **524**, 28-32.

613 Torn M.S., Trumbore S.E., Chadwick O.A., Vitousek P.M. and Hendricks D.M. (1997) Mineral

614   control of soil organic carbon storage and turnover. *Nature* **389**, 170.

615 Vogel C., Mueller C.W., Hoschen C., Buegger F., Heister K., Schulz S., Schloter M. and Kogel-

616   Knabner I. (2014) Submicron structures provide preferential spots for carbon and nitrogen

617   sequestration in soils. *Nat. Commun.* **5**, 2947.

618   Wang C.C., Chiang C.C., Liang B.Q., Yin G.C., Weng Y.T. and Wang L.C. (2017) Fast projection

619   matching for X-ray tomography. *Sci. Rep.* **7**, 3691.

620   Wang J., Xiong Z. and Kuzyakov Y. (2016) Biochar stability in soil: meta-analysis of

621   decomposition and priming effects. *Gcb Bioenergy* **8**, 512-523.

622   Weng Y.-T., Wang C.-C., Chiang C.-C., Tsai H., Song Y.-F., Huang S.-T. and Liang B. (2018) In

623   situ evidence of mineral physical protection and carbon stabilization revealed by nanoscale

624   3-D tomography. *Biogeosciences* **15**, 3133-3142.

625   Zabinsky S., Rehr J., Ankudinov A., Albers R. and Eller M. (1995) Multiple-scattering calculations

626   of X-ray-absorption spectra. *Phys. Rev. B* **52**, 2995.

627   Zbik M.S., Song Y.F. and Frost R.L. (2010) Kaolinite flocculation induced by smectite addition - A

628   transmission X-ray microscopic study. *J. Colloid Interf. Sci.* **349**, 86-92.

629   Zhu M., Hu X., Tu C., Zhang H., Song F., Luo Y. and Christie P. (2019) Sorption mechanisms of

630   diphenylarsinic acid on ferrihydrite, goethite and hematite using sequential extraction, FTIR

631   measurement and XAFS spectroscopy. *Sci. Total Environ.* **669**, 991-1000.

632

634

635 Figure 1. (**A**) Powder X- ray diffraction patterns of BC, ADE and adj. soil. (**B**) The concentrations of

636 ammonia oxalate extractable poorly crystalline Al/Fe minerals in ADE and adj. soil.

637

638 Figure 2. The SEM-BSE image and the elemental maps of BC by EDS.

639

640 Figure 3. (**A**)The TXM mosaic image for BC. (**B**)The high resolution TXM micrograph for selected

641 region. (**C**)The 3-D rendering image of organo-mineral consortium. The cross-section image exported

642 from X-ray 3-D tomography dataset along *Y-Z* plane (**D**) and along *X-Z* plane (**E**). The yellow arrow

643 in (**A**) points out the tracheid cell with mineral coating within BC. The mineral layer and BC structure

644 are shown in rouge and grey respectively in (**C**). The gold nanoparticle for alignment is shown in

645 yellow. Note that the intensity in (**D**) and (**E**) has been inversed to highlight the distribution of

646 minerals in grey. The red arrow points out the mineral clusters and layers with distinct brightness,

647 compared to the carbonaceous structure. The interface of organo-mineral is marked by the green

648 arrow in (**E**).

649

650 Figure 4. (**A**) The OM micrograph for BC. (**B**) The close-up OM micrograph for analyzed region.

651 (**C**) The X-ray diffraction pattern of the selected area in the BC. (**D**) The total intensity of diffraction

652 map of BC. The fluorescent map of Fe (**E**) and Ca (**F**) for selected area in the BC. The red and cyan

653 line index kaolinite and goethite, respectively in (**C**). The black dot square indicates the selected area

654 for fluorescent analysis where is approximately same as the field of view in (**B**). The selected area

655 bound by black dash square in (**E**) is chosen for micro-diffraction analysis.

656 Figure 5. (**A**)The FTIR spectra of BC, ADE and adj. soil. (**B**) The OM micrograph for FPA-FTIR

657 analyzed region in BC and the integral map of selected frequency range, showing the distribution of

658 the aromatic C-H over 1625-1595 cm^{-1} (**C**), carbonyl C=O over 1730-1650 cm^{-1} (**D**) and lattice water

659 O-H over 3750-3550 cm^{-1} in clay minerals (**E**), respectively.

660 Figure 6. The flowchart of mineral weathering, crystalline and transformation and proposed

661 mechanisms of organo-mineral interactions between BC and SRO minerals.

662

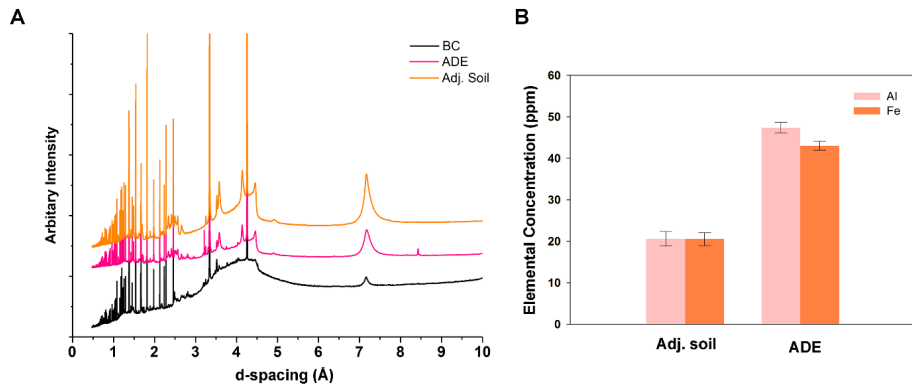663 **List of Tables**

A

B

Figure 1. (A) Powder X- ray diffraction patterns of BC, ADE and adj. soil. (B) The concentrations of ammonia oxalate extractable poorly crystalline Al/Fe minerals in ADE and adj. soil.
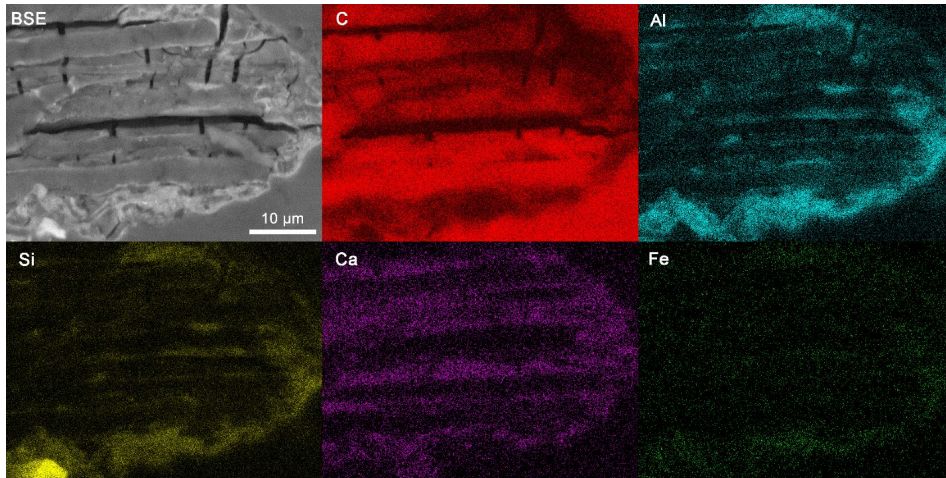
Figure 2. The SEM-BSE image and the elemental maps of BC by EDS. Left-side top corner of each square denotes Back Scattered Electron (BSE) image and specific element mapped.
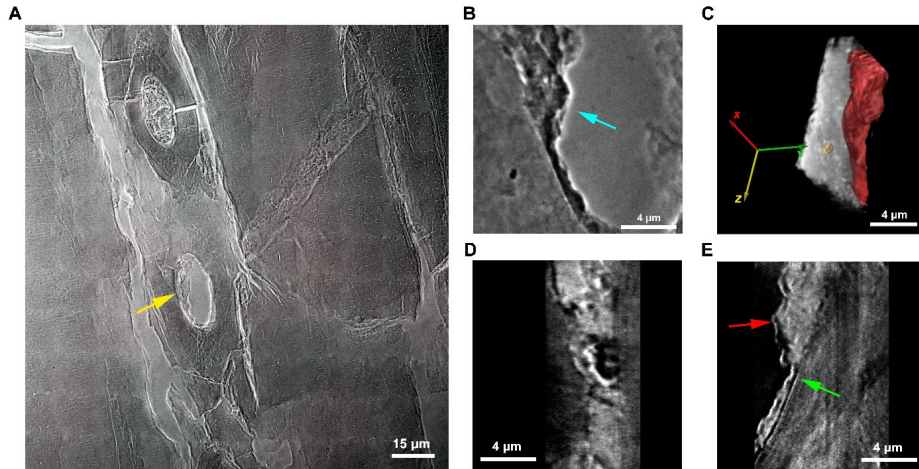
Figure 3. (A) The TXM mosaic image for BC. (B)The high resolution TXM micrograph for selected region. (C)The 3-D rendering image of organo-mineral consortium. The cross-section image exported from X-ray 3-D tomography dataset along *Y-Z* plane (D) and along *X-Z* plane (E). The yellow arrow in (A) points out the tracheid cell with mineral coating within BC. The mineral layer and BC structure are shown in rouge and grey respectively in (C). The gold nanoparticle for alignment is shown in yellow. Note that the intensity in (D) and (E) has been inversed to highlight the distribution of minerals in grey. The red arrow points out the mineral clusters and layers with distinct brightness, compared to the carbonaceous structure. The interface of organo-mineral is marked by the green arrow in (E).

Commented [W使1]: In main text, in D, sees only minerals, shows heterogeneity and porosity
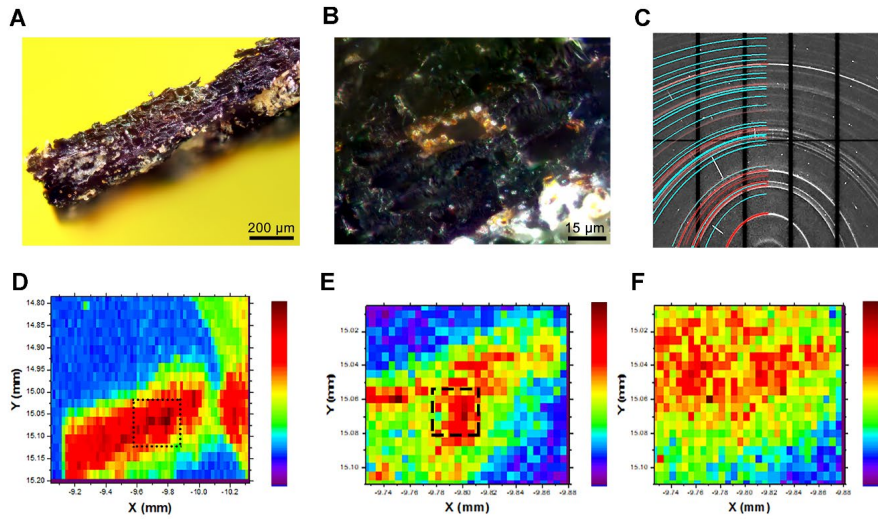
Figure 4. The OM micrograph for BC (A). The close-up OM micrograph for analyzed region (B). The X-ray diffraction pattern of the selected area in the BC (C). The total intensity of diffraction map of BC (D) and the fluorescent map of Fe (E) and Ca (F) for selected area in the BC. The red and cyan line index kaolinite and goethite, respectively in (C). The black dot square indicates the selected area for fluorescent analysis where is approximately the same as the field of view in (B) and (E). The selected area bound by black dash square in (E) is chosen for micro diffraction analysis, which was a Fe hot spot.
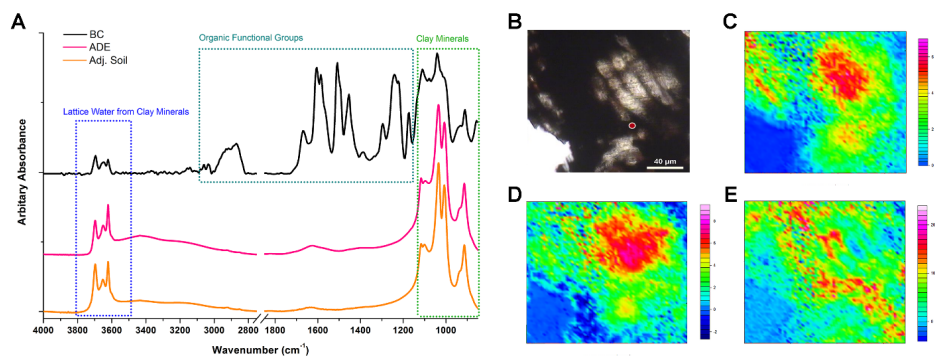
Figure 5. (A)The FTIR spectra of BC, ADE and adj. soil. (B) The OM micrograph for FPA-FTIR analyzed region in BC and the integral map of selected frequency range, showing the distribution of the aromatic C-H over 1625-1595 cm^{-1} (C), carbonyl C=O over 1730-1650 cm^{-1} (D) and lattice water O-H over 3750-3550 cm^{-1} in clay minerals (E), respectively.
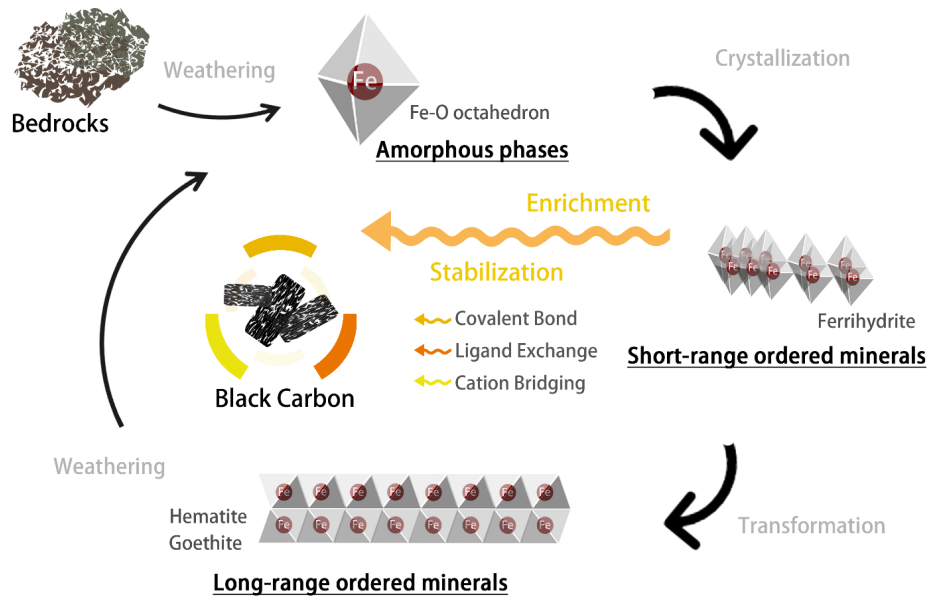
Figure 6. The flowchart of mineral weathering, crystalline and transformation and proposed mechanisms of organo-mineral interactions between BC and SRO minerals.

Table 1. The LCF result of Fe-EXAFS over the k-range of 2.9-11.3 Å^{-1} for BC, ADE and adj. soil.

LCF (K)	FERRIHYDRITE (%)[A]	GOETHITE (%)[a]	HEMATITE (%)[a]	R-FACTOR[b]
BC	80.9 (2.8)		19.8 (2.6)	0.0351
ADE	51.5 (3.8)	28.0 (5.4)	20.5 (6.6)	0.0459
Adj	53.2 (2.7)	46.8 (3.9)		0.0247

[a] The standard deviation was included in parentheses. Only the best fits are presented here.
[b] The R-factor is the normalized sum of squared residuals of the fit, $\sum(data\text{-}fit)^2/\sum data^2$

Table 2. The fitting result of Fourier transformed Fe- EXAFS over the k-range of 2.5-11.4 Å^{-1} for BC, ADE and adj. soil. [a]

PATH		CN	R (Å)	Σ^2 (Å^2)
Fe-O				
(SS)[b]	BC	6	1.98(0.01)	0.009(0.001)
	ADE	6	1.97(0.02)	0.010(0.002)
	Adj. soil	6	1.98(0.01)	0.011(0.001)
Fe-Fe[1]				
(SS)	BC	2.36(0.51)	2.98(0.01)	0.008(0.004)
	ADE	1.68(0.56)	2.98(0.02)	0.007(0.003)
	Adj. soil	1.81(0.32)	3.00(0.01)	0.008(0.002)
Fe-Fe[2]				
(SS)	BC	1.30(0.65)	3.41(0.04)	0.009(0.004)
	ADE	0.47(0.40)	3.38(0.06)	0.003(0.018)
	Adj. soil	1.80(0.43)	3.36(0.03)	0.008(0.004)

[a] Paths used in this fitting are single scattering (SS) path. S_0^2, the amplitude reduction factor, is fixed at 0.83, which is based on Fe-O first-shell fitting of hematite. The R-factor, the normalized sum of squared residuals of the fit is 0.027 for BC, 0.013 for ADE and 0.010 for adj. soil, respectively.
[b] The coordination number (CN) is fixed at 6.0.